Performance Comparison Between Optical Wireless and mmWave/THz RF Communications Systems

Iyab Sakhnini, *Senior Member, IEEE*, and Dominic O'Brien, *Member, IEEE*

***Abstract*—Radio-frequency (RF) systems are employing higher carrier frequencies (into the THz bands) leading to more limited link budgets. Above a particular RF carrier frequency, optical wireless communications (OW) systems can have a more favourable link budget, due to the different frequency dependence of signal propagation. In this paper, we present a study that estimates the RF carrier frequency at which this occurs, referred to as the cross-over RF frequency. The results show that there exists a cross-over RF frequency above which the OW system outperforms the RF system in terms of BER, which under LED background light can be as low as a few hundreds of GHz. Different receivers and background lighting conditions are also considered. A silicon photomultiplier (SiPM) detector is shown to outperform an avalanche photodiode (APD) detector in this background light conditions, while the latter becomes superior in higher sunlight conditions emphasising the crucial need for an optical filter for the SiPM.**

***Index Terms*—APD, cross-over RF frequency, mmWave, optical wireless communication, PAM, SiPM, SPAD, THz.**

I. INTRODUCTION

THE ever-increasing demand for higher data rates is motivating research for new techniques to satisfy the needs for existing and new wireless use cases [1]. In the radio frequency (RF) spectrum, the channel bandwidth available generally increases with increasing carrier frequency. The mobile wireless industry (e.g., ETSI 3GPP 5G) has been increasing the operating carrier frequency to release more spectrum, starting from sub-6 GHz to around 30 GHz and recently up to 71 GHz [2]. In 6G systems, studies investigating increasing the carrier frequency to the upper millimetre wave (mmWave) band (e.g., 100 GHz or 300 GHz) and THz band (300 GHz to 1 THz) are underway, in order to achieve data rates up to 1 Tbps [3]. Operating in these high carrier frequency bands poses several challenges to the design of the RF system including challenging power amplifier design and reduced energy efficiency [4]. In addition, the link budget becomes more limited due to increased free-space path loss (as highlighted by the Friis transmission formula), increased penetration losses, increased attenuation (e.g., due to rain), and increased molecular absorption [5]. This link budget limitation poses additional complexity to the transceiver implementation, for example, by requiring narrow and highly directive beams implemented using antenna arrays with extremely large numbers of elements. This in turn introduces additional complexity for beam management and channel estimation algorithms [6]. Generally, as the operating carrier frequency increases, an increase in the complexity of various transceiver components is expected. It is critical to have a balance between the demand for increased data capacity and the associated complexity.

Optical wireless communications (OW) is gaining increased research interest because of its potential advantages including the use of new and unregulated regions of the spectrum, higher available channel bandwidths, utilising less complex base-band modulation schemes, inherent security, and leveraging optical fibre technology [7].

Several comparisons between the OW and the RF systems have been reported. The signal to noise ratio (SNR) and the noise equivalent power (NEP) were compared between various OW and RF system schemes in [8] and it was found that the OW NEP is higher by up to few tens of dBs. In [9], the receiver sensitivity for a basic PIN photodetector (PD) was compared to a RF receiver showing the OW link having reasonable performance in a line-of-sight (LOS) condition but having large path losses in an indoor diffuse channel case. A channel model comparison between visible light communications (VLC) and RF links was presented in [10] and [11] for indoor scenarios and in [12] for vehicular scenarios. A hybrid OW and RF system was presented in [13] and [14].

From these comparisons, it can be deduced that a RF system has a better link budget compared to an OW system at relatively low operating carrier frequencies (e.g., lower mmWave band frequencies – around 60 GHz). However, as the RF industry moves into adopting higher carrier frequencies (e.g., upper mmWave and THz bands), the RF link budget becomes more limited. To improve this link budget and to reduce the implementation complexity, it may be advantageous to consider OW systems as an alternative. There is a particular carrier frequency (referred to as the cross-over RF frequency in this paper) where the OW system link budget becomes better than

that of the RF system. If such a cross-over RF frequency is understood for a certain condition, it can help influence the design choice between an OW and a RF system to get a more optimal performance. It is desirable to achieve as low a cross-over RF frequency as possible, mainly to reduce the overall system complexity.

As far as we are aware, there is not any existing work studying this cross-over RF frequency. In this paper we develop a generalised framework to understand this cross-over RF frequency and how it affects the performance of a link. We also introduce a framework to compare a silicon photomultiplier (SiPM) OW receiver to a RF receiver, which adds to previous comparisons which only use avalanche photodiode (APD) based OW receivers.

The cross-over RF frequency is estimated by developing OW and RF link models and comparing them using the same general parameters, namely, transmitter and receiver field of view (FOV), bit rate, number of bits per modulation symbol, distance between transmitter and receiver, and transmit power. Several choices for the OW photodetector (PD) receiver [15] are studied including APD and SiPM.

Section II of this paper introduces the general model description for the OW and the RF systems followed by sections III, IV, and V describing the details for the RF, APD, and SiPM models, respectively. The performance comparison among the systems is then presented in section VI by first developing a comparison model and defining the metrics, then presenting the performance comparisons. Section VII presents some of the main complexity and cost implementation considerations.

II. General Model Description

A common system link model for OW and RF systems is shown in Fig. 1. Data bits at a rate of R_b bps (bit duration $T_b = 1/R_b$ s) are modulated and transmitted using an average power of P_T W over a bandwidth of B Hz. Radiation from the source is emitted into a solid angle $\Delta\Omega_B$ (in sr) which is related to the 3-dB beamwidth $\Delta\theta_B$ (in rad) by $\Delta\Omega_B = \frac{\pi}{4}(\Delta\theta_B)^2$ [16]. The radiation intensity U (in W/sr) is defined as the emitted power per solid angle. The received power P_R (in W) available at the output of the receiver can be written as [16]:

$$P_R = A_{eff} L_s \tag{1}$$

where A_{eff} is the effective area (in m^2) and L_s (in W/m^2) is the received signal irradiance at a distance d (in m) from the transmitter written as [16]:

$$L_s = \frac{U}{d^2} \tag{2}$$

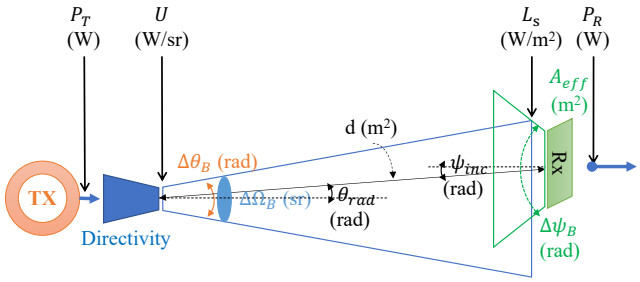

Fig. 1. Common system link model

III. RF System

A. Link Model

The radiation intensity for RF can be shown to be [16]:

$$U^{RF} = \frac{4P_T^{RF} g_T(\theta_{rad}^{RF})}{\pi(\Delta\theta_B^{RF})^2} \tag{3}$$

where θ_{rad}^{RF} is the radiation direction angle, $\Delta\theta_B^{RF}$ is the transmit beamwidth, and $g_T(\theta_{rad}^{RF})$ is the normalised antenna radiation pattern that depends on the radiation angle.

At the receiver, the antenna effective area is a function of the antenna gain G_R^{RF} and the carrier frequency f_C [16]:

$$A_{eff}^{RF} = G_R^{RF} \frac{c^2}{4\pi f_c^2} = \frac{g_R(\psi_{inc}^{RF})}{(\Delta\psi_B^{RF})^2} \frac{4c^2}{\pi f_c^2} \tag{4}$$

where ψ_{inc}^{RF} is the incident direction angle, $\Delta\psi_B^{RF}$ is the receive beamwidth, and $g_R(\psi_{inc}^{RF})$ is the normalised antenna radiation pattern that depends on the incident angle. From (2) to (4), the received power is:

$$P_R^{RF} = P_T^{RF} g_T(\theta_{rad}^{RF}) g_R(\psi_{inc}^{RF}) \left(\frac{4c}{\pi f d^{RF} \Delta\psi_B^{RF} \Delta\theta_B^{RF}}\right)^2 \tag{5}$$

B. Receiver Noise Model

The two main sources contributing to the RF noise density N_0^{RF} (in W/Hz) are thermal noise and amplifier noise [16]. Although the thermal noise can have multiple contributors, it is dominated by the noise that the antenna picks up from the environment with temperature T_A. The amplifier noise is described by the noise factor (F_N) which when expressed in dB is known as noise figure. Assuming a lossless connector and antenna, the RF receiver noise density is [16]:

$$N_0^{RF} = kF_N T_A \tag{6}$$

where k is Boltzmann's constant.

C. RF Channel Modelling

The channel in a mmWave/THz link is affected by several factors including free space propagation, molecular absorption, transmitter/receiver misalignment, multipath fading, and interference [17] and [18]. The free space propagation is

described in (5). As for molecular absorption, it is specifically caused by water vapour and oxygen leading to signal attenuation. However, for small distance links (e.g., few tens of metres), the attenuation is less than 1 dB and can be ignored (e.g., at 300 GHz, the degradation is 0.05 dB for a 10 m link) [19]. Links operating at the frequencies considered in this paper will require tracking as communications relies on good alignment between transmitter and receiver [20]. In this paper we assume that this tracking removes any losses due to misalignment.

In order to account for the high path loss at high operating carrier frequencies, the link for a mmWave/THz system is designed to be highly directional and thus has a relatively strong LOS component. However, it was shown that multipath also exists in these links which is caused by scatterers and reflected paths. This multipath small scale fading can be modelled by Rayleigh, Rician, Nakagami-m, or the more generalised $\alpha-\mu$ distribution as shown in [20] and [21]. The study in [21] shows that Rician, Nakagami-m, and the $\alpha-\mu$ distribution have very good fits compared to experimental data and are were found in [20] to be very close to each other in terms of capacity. In this paper, a Rician distribution for the multipath fading is assumed, and an additive white Gaussian noise (AWGN) channel (without fading) is included to understand how fading impacts the results. Fading however may have a severe impact on the performance of the link caused by deep fades. Diversity is used to mitigate this effect and some commonly used techniques include frequency, time, space, and polarisation diversities [22]. In this paper, we assume receive diversity with order = 2 (i.e., 2 receive RF chains) which is a commonly used technique in practice. For mmWave/THz, this is usually accomplished by utilising cross-polarised antenna panels, where each polarisation has a separate RF chain.

Interference in a mmWave/THz system is largely determined by the directivity of the transmit and receive antennas. For highly directive antennas, which is the case for mmWave/THz, any interference may be directed away from the receiver and may not be largely in the FOV of the receiver thus limiting the degradations. The study in [18] shows that although directivity increases the interference, it also increases the signal hence having limited losses for directive links. In addition, practical mmWave system designs (e.g., 3GPP 5G NR) depend on time-division multiplexing (TDM) of users which further limits any interference effects. Therefore, in this paper, the effects of interference are ignored.

D. Performance Metrics

For modulation order M_o and bit rate R_b^{RF} bps (symbol rate $R_s^{RF} = R_b^{RF}/\log_2 M_o$), the average SNR per symbol is:

$$\gamma_{avg}^{RF} = \frac{P_R^{RF}}{N_0^{RF} R_s^{RF}} \tag{7}$$

where P_R^{RF} is defined in (5) and is the average received power over all modulation symbols. Assuming Gray coding, the BER (P_b^{RF}) calculations are presented in Appendix II.

IV. OW Receiver System With APD

A. Link Model

The Lambertian intensity model is widely used to model the radiation pattern for an optical source. The radiation intensity (in W/sr) for a transmitted power of P_T^{OW} can be written as [23]:

$$U^{OW} = P_T^{OW} \frac{n+1}{2\pi} \cos^n \theta_{rad}^{OW} \tag{8}$$

where θ_{rad}^{OW} is the radiation angle and n is the Lambertian emission order related to the beamwidth $\Delta\theta_B^{OW}$ by [23]:

$$n = -\frac{1}{\log_2\left(\cos\frac{\Delta\theta_B^{OW}}{2}\right)} \tag{9}$$

To avoid the need for a perfect alignment with the transmitter, a good receiver would have a wide FOV. In addition, to have a high receiver bandwidth, a small detector capacitance is required, leading to the need for a small detector area A_d, i.e., the light needs to be focused onto as small a photodetector as possible. To achieve this, a concentrator with refractive index n_e is used to concentrate the light from a larger collection area A_{coll} into the smaller detector area A_d as shown in Fig. 2. The concentrator's gain can be written as [23]:

$$G_C = \alpha_C \frac{n_e^2}{\sin^2 \frac{\Delta\psi_B^{OW}}{2}} \tag{10}$$

where $\Delta\psi_B^{OW}$ is the receiver full FOV angle and α_C is a gain reduction factor. The effective area of the OW receiver depends on the collection area ($A_{coll} = G_C A_d$) and the angle of incidence (ψ_{inc}^{OW}) of the incoming radiation:

$$A_{eff}^{OW} = A_{coll} \cos\psi_{inc}^{OW} = \frac{A_d \alpha_C n_e^2 \cos\psi_{inc}^{OW}}{\sin^2 \frac{\Delta\psi_B^{OW}}{2}} \tag{11}$$

From (1), (2), (8), and (11), the received optical power is:

$$P_R^{OW} = P_T^{OW} \alpha_C n_e^2 \frac{(n+1)A_d}{2\pi (d^{OW})^2} \frac{\cos^n \theta_{rad}^{OW} \cos\psi_{inc}^{OW}}{\sin^2 \frac{\Delta\psi_B^{OW}}{2}} \tag{12}$$

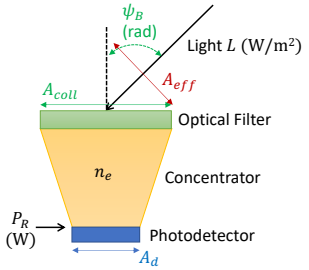

Fig. 2. OW receiver concentrator

B. Receiver Noise Model

The OW APD receiver noise sources are expressed as current sources in shunt with the received current (I_{photo}) as shown in

Fig. 3 [8] (R_L is a load resistor and C_j is the photodetector capacitance).

I_{photo} consists of the signal current I_{sig}, the dark current I_d, and the background light current I_{bg} and can be written as:

$$I_{photo} = M^2F\left(I_{sig} + I_{dg} + I_{bg}\right) + I_{ds} \tag{13}$$

where M is the APD amplification factor, F is an excess noise factor for the APD, $I_{sig} = RP_R^{OW}$ (R is the responsivity of the photodetector (in A/W)), $I_{bg} = RP_B^{OW}$ (P_B^{OW} is the power for the sum of all background light sources which reaches the PD). I_{ds} (surface leakage current) and I_{dg} (substrate current) are the two components of the dark current ($I_d = I_{ds} + MI_{dg}$) [24]. F is a function of M and the ionisation rate ratio (k_i) [24]:

$$F = Mk_i + \left(2 - \frac{1}{M}\right)(1 - k_i) \tag{14}$$

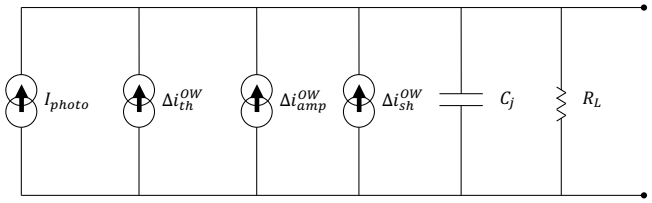

Fig. 3. OW PIN/APD equivalent electrical model

The noise sources for an APD receiver are mainly thermal noise, amplification noise, and shot noise. Thermal noise is described as the current due to the equivalent load resistor (R_L) connected to the photodetector with density expressed as $J_{sh} \triangleq (\Delta i_{th}^{APD})^2 = \frac{4kT_{res}^{APD}}{R_L}$ (in A^2/Hz) where T_{res}^{APD} is the temperature of the resistor [25]. Amplification noise can be characterised as $J_{amp} \triangleq \left(\Delta i_{amp}^{APD}\right)^2 = a^2$, where a is the amplifier noise (in $A/\sqrt{Hz}$). The shot noise density can be expressed as $J_{sh} \triangleq (\Delta i_{sh}^{APD})^2 = 2qI_{photo}$ (in A^2/Hz) [25], where q is the elementary charge. Due to the signal dependent nature of shot noise, it is often small relative to the thermal noise at room temperature and low to moderate received powers, while it can dominate at very low operating temperatures and/or for high received power levels. The total OW receiver noise density (in A^2/Hz) can be written as: $J^{APD} = J_{th} + J_{amp} + J_{sh}$. Ignoring the dark current ($I_{dg} = I_{ds} \approx 0$) by assuming it is much smaller than the signal, the noise density can be written as a function of the signal and background intensities, L_S^{OW} and L_B^{OW}, respectively as:

$$J^{APD} = \frac{4kT_{res}^{APD}}{R_L} + a^2 + F_{shot}(L_S^{OW} + L_B^{OW}) \tag{15}$$

where $F_{shot} \triangleq 2qM^2FRA_{eff}^{OW}$.

C. Performance Metrics

The electrical SNR calculations for OW and RF differ in the way the electrical power is calculated. The RF electrical power is the received power P_R^{RF}, while for OW, it depends on the electrical current after the photodetector (I_{sig}^2). For bit rate R_b^{OW} bps (symbol rate $R_s^{OW} = R_b^{OW}/\log_2 M_o$), the APD electrical SNR for the m^{th} modulation symbol ($m \in \{0, \dots, M_o - 1\}$) with received signal power $P_R^{OW}[m]$ and noise density $J^{APD}[m]$ can be written as:

$$\gamma^{APD}[m] = \frac{(MRP_R^{OW}[m])^2}{J^{APD}[m]R_S^{OW}} \tag{16}$$

For OOK, the BER as a function of SNR is [25]:

$$P_b^{APD} = Q\left(\frac{1}{2}\sqrt{\gamma^{APD}[1]}\right) \tag{17}$$

However, for higher order PAM, because of the signal dependent noise, the detection threshold for each symbol is different and using a common minimum distance between adjacent symbols for deriving the BER (similar to RF) cannot be used. Instead, a threshold based on the mean and variance of each two adjacent symbols is used. Assuming Gray coding, the BER can be approximated as [26]:

$$P_b^{APD} \approx \frac{1}{M_o \log_2 M_o}\left(\sum_{m=0}^{M_o-2}\left(Q\left(\frac{t_m - \mu_m}{\sigma_m}\right) + Q\left(\frac{\mu_{m+1} - t_m}{\sigma_{m+1}}\right)\right)\right) \tag{18}$$

where $\mu_m = \frac{MRP_R^{OW}[m]}{\sqrt{R_S^{OW}}}$, $\sigma_m = \sqrt{J^{APD}[m]}$, and the maximum likelihood detection thresholds t_m calculated by solving:

$$\log \sigma_m + \frac{1}{2}\left(\frac{t_m - \mu_m}{\sigma_m}\right)^2 = \log \sigma_{m+1} + \frac{1}{2}\left(\frac{t_m - \mu_{m+1}}{\sigma_{m+1}}\right)^2$$

V. OW Receiver System With SiPM

A. OW SiPM Receiver

A single-photon avalanche diode (SPAD) is an extremely sensitive photodetector capable of detecting a single photon achieved by biasing the PD to a value much higher than its reverse-bias breakdown voltage [27] and [28]. When a photon triggers a SPAD, an avalanche occurs generating very high current. A quenching device (active or passive) is placed in series with the SPAD to recover the bias voltage. It takes time for the bias voltage to recover during which the SPAD cannot detect any photons during a time known as the recovery (or recharge) time (τ). The recovery time can be derived from the recovery time constant (τ_{TC}) using $\tau = 2.2\tau_{TC}$ [29]. To mitigate this, an array of SPADs is used where during the recovery time of one SPAD, another one in the array can detect another photon if it arrives [28]. This array of SPADs is referred to as a silicon photomultiplier (SiPM). The ratio of the sum of all SPAD active areas to the area of the SiPM is known as the fill factor (FF).

SPADs may have several non-ideal behaviours including dark counts, after-pulsing, and optical cross-talk [28]. The dark count rate (cps: count per sec) can be written as:

$$C_{dark}^{MEAN} = f_{dark}A_{SPAD} \tag{19}$$

where f_{dark} is the dark count rate per m^2 (kHz/m^2) and A_{SPAD} is the SPAD area in m^2. After-pulsing can be excluded from the processing by implementing a pulse-height analysis or a time-delay filtering algorithm [30]. Also, in practical SiPMs, optical trenches around every SPAD are implemented which considerably reduce the optical cross-talk [30]. Hence, for the purpose of this paper, after-pulsing and optical cross-talk effects were ignored.

When a SiPM is used in photon counting mode, which is the assumption used in the paper, an amplifier, e.g., transimpedance amplifier (TIA), is not needed in the receiver circuitry eliminating the amplifier electronic noise component. This restricts the noise to be Poisson distributed with mean and variance equal to the number of photons detected (N_{ph}). As the light intensity increases, the SiPM response becomes non-linear and saturates at high intensity levels. Several non-linear response models for the SiPM have been studied and in this paper the following model was used to estimate the mean number of photons detected (N_{ph}) [31]:

$$N_{ph} = T_s N_{SPADs} \frac{\alpha(L_{dark} + L_B^{OW} + L_S^{OW})}{1 + \alpha\tau(L_{dark} + L_B^{OW} + L_S^{OW})} \tag{20}$$

where T_s is the modulation symbol duration, N_{SPADs} is the number of SPADs in the SiPM, $\alpha = \frac{\eta A_{SPAD}^G}{E_p}$, A_{SPAD}^G is the effective SPAD area (m^2) defined as $A_{SPAD}^G = G_C A_{SPAD}$ (G_C is defined in (10)), E_p is the photon energy (J), η is the photon detection probability, and L_{dark} is the equivalent mean intensity (W/m^2) representing the effect of dark counts defined as:

$$L_{dark} = C_{dark}^{MEAN} \frac{E_p}{\eta A_{SPAD}^G} \tag{21}$$

If the symbol time is shorter than the SPAD pulse width, inter-symbol interference (ISI) starts to occur and an equaliser is needed [29]. In this paper, T_s is assumed to be larger than the pulse width and an equaliser is not needed.

B. Performance Metrics

For pulse amplitude modulation (PAM), assuming the error is confined to adjacent symbols (e.g., using Gray coding), the symbol error rate (SER) between adjacent symbols n and m ($P_e^{(n,m)}$) is approximated by [32]:

$$P_e^{(n,m)} \approx \frac{P_e^{SiPM}}{M_o - 1} \approx \frac{P_b^{SiPM} \log_2 M_o}{M_o - 1} \tag{22}$$

where P_e^{SiPM} and P_b^{SiPM} are the total SER and BER, respectively. The probability of symbol error between two adjacent symbols with Poisson distributed number of photons detected with means N_n and N_m ($N_n < N_m$) is [32]:

$$P_e^{(n,m)} = \frac{1}{M_o}\left[\sum_{k=\lceil n_T \rceil}^{\infty} \frac{N_n^k}{k!} e^{-N_n} + \sum_{k=0}^{\lfloor n_T \rfloor} \frac{N_m^k}{k!} e^{-N_m}\right] \tag{23}$$

where for a maximum-likelihood detector, the threshold n_T is:

$$n_T = \frac{N_m - N_n}{\log N_m - \log N_n} \tag{24}$$

Assuming equal SER between all adjacent symbols, the received mean photon counts needed for PAM levels will not be equidistant due to the nature of the Poisson distribution where the variance increases as the mean increases, therefore increasing the inter-symbol distance as the power increases. An algorithm to iteratively calculate the PAM levels was proposed in [33] and is used in this paper.

VI. Performance Comparison

C. Comparison Model

To compare the performance of various system links, one of the typical metrics used is the average received SNR which is used to calculate the BER. For RF, the average SNR presented in (7) can be used in the BER calculations. However, for the OW APD case, the average SNR cannot be used for the BER calculations, and modulation symbol-dependent signal and noise were used instead as in (18). Additionally, for an OW SiPM system, the noise is complicated to model especially in the non-linear region of the SiPM response. While several SNR models exist [31], [34], and [35], some of them were developed for the linear region only and others were developed for a particular application or non-ideal behaviour. This led to developing the BER for the SiPM as in section V to be based on the received photon counts and not on SNR. Hence, for this comparison, the average SNR is not a good metric of comparison.

Another consideration is the receiver effective area. The RF receiver typically implements a phased antenna array or a dielectric collimating lens [5]. The OW APD receiver in this paper is assumed to be a single PD while the SiPM is assumed to be an array of SPADs. Hence, the actual physical and effective areas for these receivers vary considerably.

To compare these systems, an input that is independent of the effective area, i.e., receiver irradiance (L_s in W/m^2) and an output that is available for all three systems, i.e., SER (P_e) or BER (P_b) were considered.

For intensity modulation and direct detection (IM/DD) OW systems [36], a PAM modulation scheme was used [37]. For the RF system, two modulation scheme categories were considered: non-coherent PAM (referred to as RF MOD1) and the more power efficient coherent modulation schemes typically used in RF systems, e.g., PSK and QAM (referred to as RF MOD2) [22]. The comparison assumes modulation schemes having the same number of bits per symbol, e.g., 2-PAM compared to BPSK, etc.

For the OW receivers, parameters from commercial APD and SiPM devices were used, namely, Hamamatsu S8664-10K [39] (denoted as APD) and Onsemi J-Series SiPM 30020 [40] (denoted as SiPM-1). An optical concentrator was assumed with a refractive index of 1.5, FOV of 30°, and gain factor (α_C) of 0.5. This yields a total collection area for the SiPM-1 and APD detectors to be 156.1 mm^2 and 13.1 mm^2, respectively,

with a gain of around 16.8. To better understand the APD and SiPM comparison, an additional SiPM model was defined (denoted as SiPM-2), which is based on SiPM-1 but modified to have the same collection area as the APD (i.e., 13.1 mm^2), leading to the same received optical power. Using the same optical concentrator parameters, this reduced area resulted in the reduction of the number of SPADs in SiPM-2 to 1209 (compared to 14410 of SiPM-1).

TABLE I
STUDY ASSUMPTIONS

Tx to Rx link distance (d)	10 m
Required BER	10^{-4}
Transmitter beam width	2 deg
Receiver beam width	30 deg
RF receiver noise figure	10 dB
RF Rician channel parameter K	2
Bit rate (R_b)	500 Mbps
OW wavelength	420 nm
OW Tx/Rx alignment	Perfect alignment
OW concentrator factor (α_C)	0.5
OW concentrator refractive index (n_e)	1.5
OW optical filter bandwidth	1 nm
OW LED background light	4.2e-4 W/sr/m^2/nm
OW indoor sunlight (1200lux)	8.4e-3 W/sr/m^2/nm
OW outdoor sunlight [1]	1.8e-1 W/sr/m^2/nm

[1] Assuming hemispherical tilt irradiance numbers from [38]

To characterise the effect of background light on the OW receivers, the performance was studied under a range of background light values starting from no background light until a value corresponding to direct outdoor sunlight (assuming hemispherical tilt irradiance [38]).

Optical filtering to reduce background light is a critical element of any high-performance optical wireless system. When using a bandpass optical filter, it is desirable to have a narrow bandwidth to effectively reject background light and increase the SNR. In this study, it is also desirable to have a wide receiver FOV to reduce alignment tolerance yet maintain narrow filter bandwidth. This is not achievable using planar optical filters, due to the passband shift for off-axis angles of incidence. Such dependence can be mitigated by depositing a bandpass filter onto the outer surface of a non-imaging hemispherical concentrator [41]. In this study, an optical filter with a bandwidth of 1 nm and FOV of 30^o placed in front of the concentrator was assumed.

Detailed study assumptions are shown in Table I. A bit rate of 500 Mbps was assumed for the comparison. Both the Hamamatsu S8664-10K APD detector and the Onsemi J-Series SiPM 30020 detector can support this bit rate, where the former has a bandwidth of 530 MHz and the latter has a pulse width from the fast output of 1.4 ns capable of supporting a bit rate up to around 700 Mbps [29]. Device specifications are shown in Table IV and Table V in the appendix.

For RF fading, both an AWGN and a Rician fading channel were assumed. A Rician channel parameter K = 2 was chosen based on the average of the experimental values shown in [21], where K is the ratio of the LOS signal power to the other non-LOS signal components.

D. Cross-Over RF Frequency

The cross-over RF frequency is defined as the RF carrier frequency at which the OW system outperforms the RF system. The performance is defined by the required mean signal irradiance (L_s in W/m^2) to achieve the same BER (1e-4 assumed in this comparison) assuming the same link distance and the same transmit and receive beamwidths.

The cross-over RF frequency results as a function of the OW background light are shown for an AWGN channel in Fig. 4 for RF using PAM and in Fig. 5 for RF using coherent modulation schemes. Fig. 6 shows the same results for a RF system assuming a Rician fading channel with diversity order of 2. Table II and Table III show the cross-over RF frequencies for OW without background (BG) light and with BG LED light with irradiance of 4.2e-4 W/sr/m^2/nm (typical room lighting) for a RF system assuming AWGN and Rician channels, respectively. We can summarise the key observations as: (i) SiPM-based receivers generally outperform APD-based receivers in low to medium background light conditions and large number of SPADs, (ii) APD-based receivers have better relative performance compared to RF using PAM as modulation order increases, (iii) as background light increases, supporting higher order modulations becomes more difficult for SiPMs, (iv) improved relative performance for the SiPM-1 case compared to RF using PAM with increasing modulation order for the cases of low levels of background light, (v) using RF coherent modulation schemes improves the RF relative performance, and (vi) significant OW system relative performance improvement (lower cross-over RF frequency) compared to RF systems when assuming Rician fading as compared to AWGN channel. In the remainder of this section, a detailed analysis is provided.

The received optical power for the OW and RF systems is comparable, however, the OW electrical power is much lower mainly because the incoherent OW receiver detects power which is then converted to electric current [41]. Hence, the OW receiver's detection is based on the square of the received power and needs much higher power to achieve the same performance as that of the coherent RF receiver.

The SiPM however has the advantage of a very sensitive photon-counting detection operating in the Poisson limit. This results in much lower cross-over RF frequencies for SiPM compared to the APD receiver for low background light conditions and low modulation orders. However, increasing the background light degrades the performance of the SiPM-based systems considerably (as shown in Fig. 4 to Fig. 6) with much higher relative performance degradation compared to the APD. In high levels of background light, the APD starts outperforming the SiPM.

Compared to RF using PAM, the APD performs better as the modulation order increases (cross-over RF frequency decreases) as can be seen from the results in Table II. This is due to the better power efficiency for higher order PAM for APD compared to RF using PAM mainly because the transmitted signal input to the OW channel is power and not

amplitude as in the RF case [41]. However, when compared to RF using the more power efficient schemes, the APD performs worse with increasing modulation order, as indicated by an increase in cross-over frequency.

TABLE II
CROSS-OVER RF FREQUENCY (GHZ)
AWGN CHANNEL

BG Light	Mod order	APD		SiPM-1		SiPM-2	
		RF MOD 1	RF MOD 2	RF MOD 1	RF MOD 2	RF MOD 1	RF MOD 2
No	2	4005	5664	203	288	665	940
	4	3442	8927	221	574	1185	3073
	8	3007	9535	242	769	N/A	N/A
	16	2766	14880	355	1910	N/A	N/A
Yes (Note 2)	2	4007	5667	426	603	1214	1717
	4	3443	8930	378	981	N/A	N/A
	8	3008	9537	365	1157	N/A	N/A
	16	2766	14881	N/A	N/A	N/A	N/A

- Note 1: Number of SPADs: SiPM-1 = 14410, SiPM-2: 1209
- Note 2: LED lighting assumed 4.2e-4 W/sr/m^2/nm

TABLE III
CROSS-OVER RF FREQUENCY (GHZ)
RICIAN CHANNEL ($L = 2$, $K = 2$)

BG Light	Mod order	APD	SiPM-1	SiPM-2
		RF MOD2	RF MOD2	RF MOD2
No	2	2378	121	395
	4	3747	241	1290
	8	4236	342	NaN
	16	6500	834	NaN
Yes (Note 2)	2	2379	253	721
	4	3748	412	NaN
	8	4237	514	NaN
	16	6500	NaN	NaN

- Note 1: Number of SPADs: SiPM-1 = 14410, SiPM-2: 1209
- Note 2: LED lighting assumed 4.2e-4 W/sr/m^2/nm

For the SiPM, the number of photons detected increases linearly with the number of SPADs as shown in (20), therefore, SiPM-1 has better performance compared to SiPM-2 due to the larger number of SPADs. This can be seen from the results in Table II and Table III. As the background light increases, the SiPM non-linearity becomes a major factor in degrading the performance. This can be noted from the significant increase in the crossover RF frequencies for both SiPMs as the background light increases (Fig. 4 to Fig. 6). Due to the smaller number of SPADs, SiPM-2 becomes saturated at a much lower irradiance and its performance degrades faster than SiPM-1. Fig. 7 shows the response and 4-PAM modulation symbols for both SiPMs. As can be seen, the third and fourth modulation symbols are in the saturated region for SiPM-2.

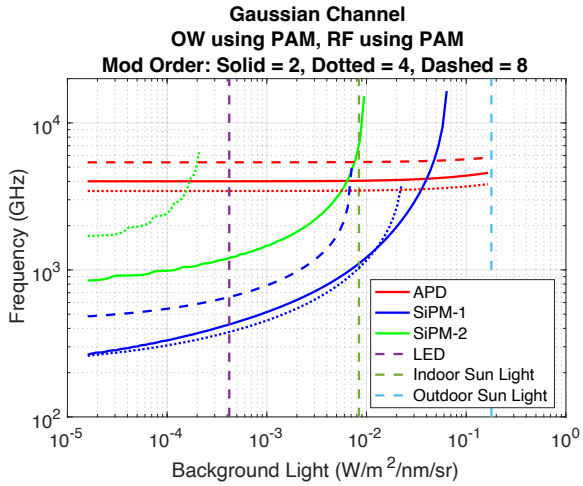

Fig. 4. Cross-over RF frequency for AWGN channel (RF MOD1)

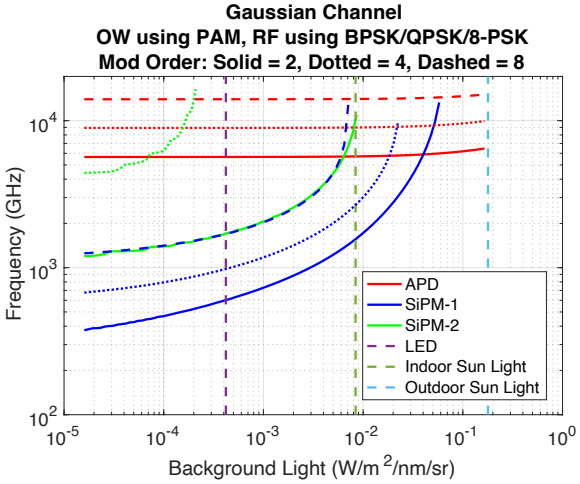

Fig. 5. Cross-over RF frequency for AWGN channel (RF MOD2)

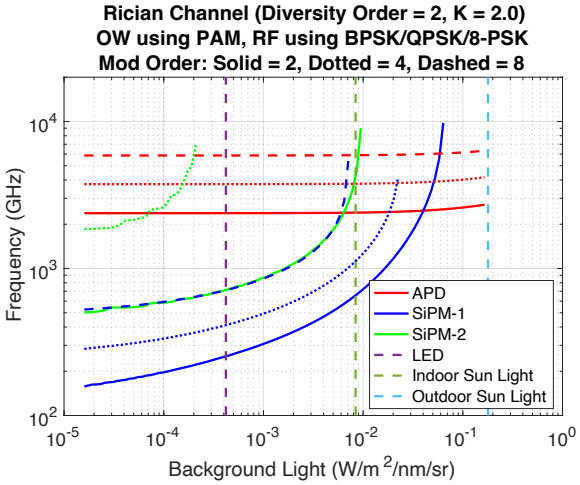

Fig. 6. Cross-over RF frequency for Rician channel ($\boldsymbol{K}$ = 2) with diversity order = 2 (RF MOD2)

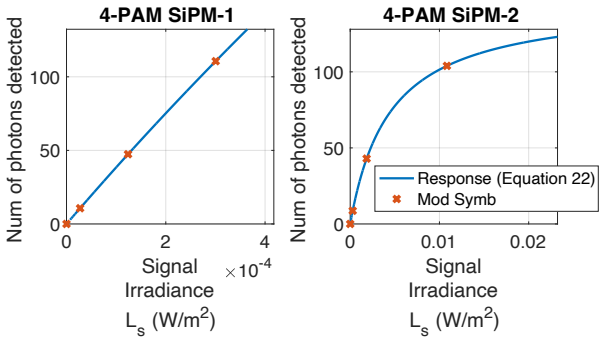

Fig. 7. SiPM number of photons detected versus irradiance

From the results in Table II and Table III, it can be seen that it is more difficult to support higher modulation orders using the SiPMs. For SiPM-1, 16-PAM can only be supported in the case without background light. SiPM-2 can only support modulation schemes up to 4-PAM in cases without background light, and only OOK (2-PAM) in cases with some background light. This is because the higher order modulation symbols get deeper into the saturation region and thus no matter how much the signal irradiance for these symbols is increased, there is not enough difference in the number of photons counted to achieve the required BER. Hence, the respective modulation order cannot be supported.

These observations indicate the critical need for using an optical filter especially for the SiPM-based detector. For practical design considerations, the filter needs to have a wide enough FOV to avoid the need for complex link alignment challenges and needs to have a narrow bandwidth to limit the background light.

Fig. 8 shows a comparison of the mean required irradiance between the SiPM and RF using PAM cases. The left plot shows the absolute mean required irradiances, the centre plot shows the mean required irradiance difference between different PAM modulation levels, and the right plot shows the mean required irradiance difference between adjacent levels of 16-PAM. From the centre plot of Fig. 8, it can be seen that increasing the modulation order requires a slightly higher mean required irradiance for SiPM-1 without background light as compared to RF, hence the slight degradation in the relative performance as in Table II. On the other hand, the saturated higher order modulation for SiPM-2 decreased its performance relative to RF (cross-over RF frequency increasing). When compared to the more power efficient RF modulation schemes, the power advantage for the higher order RF modulation schemes leads to worse performance relative to RF as modulation order increases for both SiPM receivers.

An interesting observation from Fig. 4 is the improved relative performance for the SiPM-1 case compared to RF using PAM with increasing modulation order for the cases of low levels of background light (< 3e-3 W/sr/m^2/nm). This can be explained by the following. As the absolute mean irradiance level increases as modulation order increases (left plot of Fig. 8), the rate of this increase is almost the same for RF and SiPM-1 without background light (centre plot of Fig. 8). However, the rate of this increase for the SiPM with background light is less compared to the RF system (centre plot of Fig. 8) leading to better relative performance as modulation order increases. This can be explained by the nature of the Poisson distribution, where the difference between the required irradiances of the adjacent PAM levels become smaller with additional background light (right plot of Fig. 8). However, as the background light increases (> 3e-3 W/sr/m^2/nm), higher order modulations will be affected by the saturation of the SiPM-1 hence the worse performance compared to lower order modulations.

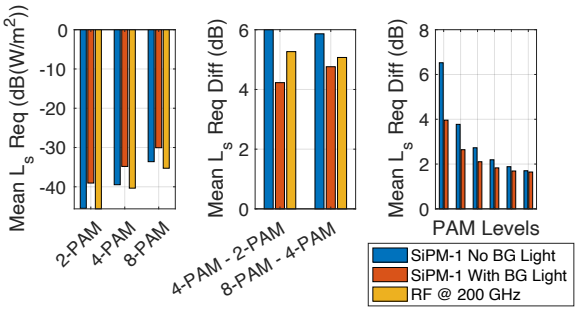

Fig. 8. Left: Mean L_s Req. Centre: Mean L_s Req Difference. Right: Mean L_s Req Diff Between 16-PAM Levels. BG light refers to LED lighting at 4.2e-4 W/sr/m^2/nm

E. Power Penalty

In addition to the cross-over RF frequency, we can also study the power penalty, defined as the additional average power needed for the OW to have the same BER performance (e.g., 1e-4) as that of RF, as shown in Fig. 9 for the Rician fading channel case. The RF systems assumed to use carrier frequencies based on the cross-over RF frequency with no background light for each modulation for SiPM-1 (from Table III). As previously observed, the background light has a much higher impact on the relative performance for SiPM compared to APD. For SiPM-1, the power penalty can be as large as 7 dB for an indoor LED case.

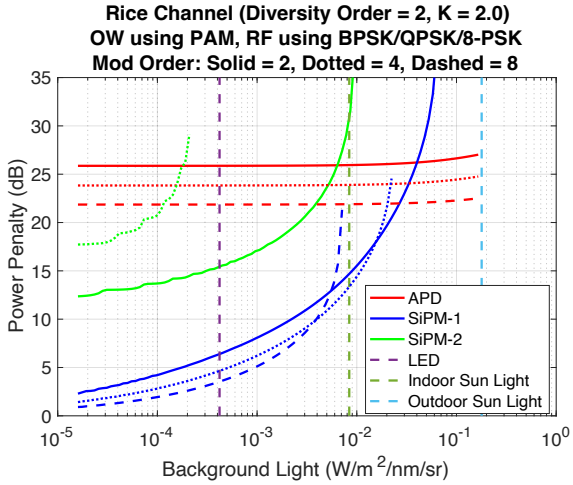

Fig. 9. OW power penalty for Rician channel (K = 2) with diversity order = 2 (RF2)

VII. Design Considerations

A. Supported Communications Bandwidth

The study focuses on the comparative link budget for 500 Mb/s OW and RF links, with the required bandwidth varying according to the modulation schemes chosen.

The bandwidth that is *potentially* available for communications is markedly different for OW and RF, due to the difference in wavelength, with OW providing spectrum a few orders of magnitude larger than the RF spectrum [7].

However, both for OW and RF systems there are often limiting practical considerations in accessing this spectrum. Most OW systems, including the case considered here, use (IM/DD) approaches [47]. Such systems are simple, as there is no requirement for carrier demodulation at the receiver. For both IM/DD and coherent systems there is typically a compromise between the modulation bandwidth of the transmitter source and the power it emits, with faster devices operating at lower power levels. At the receiver, the relationship between bandwidth and detection area is technology dependent, with larger detection area typically leading to lower bandwidth. Achieving 'full' access to the available optical spectrum is therefore challenging (see [7] for a fuller discussion, and [15] for a review of the particular transmitter and receiver technology options.

For RF communications, operating in the sub-THz and THz spectrum regions provides higher available communications bandwidths. However, operating at such high carrier frequencies with larger bandwidths poses several implementation challenges. Designing high resolution digital-to-analogue (DAC) and analogue-to-digital (ADC) converters at very high sampling rates is a key challenge for THz RF systems limiting the communications bandwidth that can be supported. Supporting high sampling rates (e.g., 100 Giga sample per second) has been demonstrated but at the expense of resolution, power, and area [42]. A 3GPP 5G study has shown a linear dependency between the channel bandwidth and the complexity/cost of the ADC/DAC [43]. Using lower resolution ADCs/DACs helps mitigate some of this complexity but comes with its own design challenges and needs [44]. Another way to mitigating this complexity is by dividing the channel into multiple narrower sub-channels and using multiple ADCs/DACs [45]. In addition to the ADC/DAC design challenges, higher channel bandwidth increases the design complexity of channel linearisation techniques like envelope tracking and digital pre-distortion (DPD) [46].

B. Other Complexity Considerations

For OW communications, there are generally two types of communications namely incoherent (IM/DD) and coherent [47]. The latter type is spectrally more efficient; however, it requires the use of local oscillators, optical mixers, and other components at the receiver making it more complex and costly compared to the much simpler IM/DD system. For the IM/DD systems considered here the components required are used for a number of different applications, making them widely available and reliable (albeit not always optimised for OW). The SiPM devices considered here are newer technology and are finding wide application in 3D sensing and LIDAR. These SiPMs consist of a large number of detectors (pixels) wired in parallel. In CMOS image sensors there are always a few pixels, known as dead pixels, which don't respond to light. However, these don't impact the sensor yield because their response can be estimated from the response of equivalent neighbouring pixels. This precedent suggests that a few microcells per SiPM won't respond to photons. If the SiPM is used in an imaging application these few faults can be corrected and so they will reduce the yield of single photon imaging sensors. However, if the SiPM is used in a non-imaging mode any faulty microcells will simply reduce the effective photosensitive area of the SiPM and hence its PDE. Since a typical SiPM has more than a thousand microcells the resulting variation in PDE will be smaller than the variation between PDEs of different SiPMs due to effects such as the variation in breakdown voltage. Cost of CMOS devices such as SiPMs is largely governed by device area, so area minimisation will likely be a concern in mass-market applications.

For RF, in addition to the additional complexity of ADC/DAC design as explained in the previous section, operating at high carrier frequency bands poses challenges related to power amplifier design and reduced energy efficiency, increased phase noise, and reduced link budget. The main challenge for power amplifier design for THz communications is to balance cost (e.g., by using silicon-based amplifiers) and performance (e.g., by using III-V compound semiconductor families) especially when using waveforms requiring high peak-to-average-power (PAPR) ratio [46]. Increased phase noise, caused by inaccuracies of the local oscillators at the transmitter and receiver, can be mitigated by several techniques including better (more expensive) oscillators and digital signal processing techniques [46].

VIII. Conclusion

As higher carrier frequencies are being considered for the RF-based systems (reaching the THz bands), it becomes critical to develop a framework for comparing OW and RF systems which can help answer questions about what system to use in which scenario. One of the important metrics for this comparison is the cross-over RF frequency after which the OW system outperforms the RF system in terms of BER for the same transmit power and link distance. It is important to have as low cross-over RF frequency as possible to avoid the high complexity of the high carrier frequency RF system design.

In this paper, a framework was developed to find this cross-over RF frequency. Two categories of OW receivers were considered in this study based on either APD and SiPM. The effect of the background light on the performance of the OW system was also studied. A SiPM-based system assuming no background light was shown to outperform, in terms of BER, a RF-based system assuming an AWGN channel using carrier frequencies as low as 200 GHz. This cross-over RF carrier

frequency decreases to around 120 GHz if a Rician fading channel with parameter = 2 and diversity order of 2 was assumed for the RF system. A typical LED indoor background light scenario can increase the cross-over RF frequency to around 300-1100 GHz for AWGN RF channel and to around 250-500 GHz for a Rician RF channel depending on the modulation order and scheme. To achieve the same cross-over RF frequency as the no background light case, an additional 7 dB average OW transmit power is needed. For the same diversity order, increasing the LOS component ratio of the Rician channel (increasing K) would bring the performance closer to the AWGN case. It was also noted the better relative performance of the OW system compared to RF using PAM as the modulation order increases for APD and for SiPM with little background lighting. It was also shown that higher order modulation schemes cannot be supported by the SiPM for higher background lighting conditions (e.g., sunlight) highlighting the critical need of using an optical filter for a SiPM-based receiver.

Therefore, depending on the scenario and background lighting cases, OW communication systems can have a comparable performance in terms of BER as RF systems in the upper mmWave band (100 GHz to 300 GHz) and THz spectrum (300 GHz to 1 THz) regions. This can be used to design better performing and less complex systems by considering OW as an alternative to RF for these higher frequency regions.

APPENDIX I

TABLE IV
OW APD PARAMETERS

Commercial part	Hamamatsu S8664-10K **[39]**
PD area (A_d)	0.78 mm^2
Amplification factor (M)	50
Bandwidth	530 MHz
Responsivity (R)	0.24 A/W
Dark current (I_d)	0.3 nA
Amplifier noise (a)	0
Collection area (A_{coll})	13.1 mm^2

TABLE V
OW SIPM PARAMETERS

	SiPM-1	**SiPM-2**
Commercial part	Onsemi J-Series 30020 [40]	N/A
SPAD pitch	20 µm	20 µm
Number of SPADs (N_{SPADs})	14410	1209
Fill factor (FF)	0.62	0.62
Photon detection efficiency (PDE)	0.3	0.3
Photon detection prob. (η = PDE/FF)	0.48	0.48
Recovery time constant (τ_{TC})	15 ns	15 ns
Pulse width	1.4 ns	1.4 ns
Dark count rate	50 kHz/mm^2	50 kHz/mm^2
Collection area/SPAD (A_{coll})	0.0067 mm^2	0.0067 mm^2
Total coll. area ($A_{total} = \frac{N_{SPADs}A_{coll}}{FF}$)	156.1 mm^2	13.1 mm^2

APPENDIX II

In this paper, two RF link channel models were assumed, namely AWGN and Rician (with receiver diversity order L = 2 and parameter K = 2). Simulations were used for the BER for the Rician channel, while the following closed form formulae were used for AWGN [22]:

AWGN single polarity PAM:

$$P_b^{RF} \approx \frac{2(M_o-1)}{M_o \log_2 M_o}\, Q\left(\sqrt{\frac{3}{(M_o-1)(2M_o-1)}\gamma_{avg}^{RF}}\right) \tag{25}$$

AWGN PSK modulation:

$$P_b^{RF} \approx \frac{2}{\log_2 M_o}\mathrm{Q}\left(\sqrt{2\sin^2\left(\frac{\pi}{M_o}\right)\gamma_{avg}^{RF}}\right) \tag{26}$$

AWGN QAM modulation:

$$\begin{aligned} P_b^{RF} &\approx \frac{4}{\log_2 M_o}u(1-u) \\ &\leq \frac{4}{\log_2 M_o}\mathrm{Q}\left(\sqrt{\frac{3}{M_o-1}\gamma_{avg}^{RF}}\right) \end{aligned} \tag{27}$$

where $u = \left(1-\frac{1}{\sqrt{M_o}}\right)\mathrm{Q}\left(\sqrt{\frac{3}{M_o-1}\gamma_{avg}^{RF}}\right)$ and $\mathrm{Q}(\cdot)$ is standard normal distribution tail function.

REFERENCES

[1] M. Giordani, M. Polese, M. Mezzavilla, S. Rangan, and M. Zorzi, "Toward 6G Networks: Use Cases and Technologies," *IEEE Communications Magazine,* vol. 58, no. 3, pp. 55-61, 2020, doi: 10.1109/MCOM.001.1900411.

[2] A. Ghosh, A. Maeder, M. Baker, and D. Chandramouli, "5G Evolution: A View on 5G Cellular Technology Beyond 3GPP Release 15," *IEEE Access,* vol. 7, pp. 127639-127651, 2019, doi: 10.1109/ACCESS.2019.2939938.

[3] M. A. Uusitalo *et al.*, "6G Vision, Value, Use Cases and Technologies From European 6G Flagship Project Hexa-X," *IEEE Access,* vol. 9, pp. 160004-160020, 2021, doi: 10.1109/ACCESS.2021.3130030.

[4] T. S. Rappaport *et al.*, "Wireless Communications and Applications Above 100 GHz: Opportunities and Challenges for 6G and Beyond," *IEEE Access,* vol. 7, pp. 78729-78757, 2019, doi: 10.1109/ACCESS.2019.2921522.

[5] K. Rikkinen, P. Kyosti, M. E. Leinonen, M. Berg, and A. Parssinen, "THz Radio Communication: Link Budget Analysis toward 6G," *IEEE Communications Magazine,* vol. 58, no. 11, pp. 22-27, 2020, doi: 10.1109/MCOM.001.2000310.

[6] J. Gao, C. Zhong, G. Y. Li, J. B. Soriaga, and A. Behboodi, "Deep Learning-Based Channel Estimation for Wideband Hybrid MmWave Massive MIMO," *IEEE Transactions on Communications,* vol. 71, no. 6, pp. 3679-3693, 2023, doi: 10.1109/TCOMM.2023.3258484.

[7] H. Haas, J. Elmirghani, and I. White, "Optical wireless communication," *Philosophical Transactions of the Royal Society A: Mathematical, Physical and Engineering Sciences,* vol. 378, no. 2169, p. 20200051, 2020/03/02 2020, doi: 10.1098/rsta.2020.0051.

[8] G. Morthier, G. Roelkens, and R. Baets, "Optical Versus RF Free-Space Signal Transmission: A Comparison of Optical and RF Receivers Based on Noise Equivalent Power and Signal-to-Noise Ratio," *IEEE Journal of Selected Topics in Quantum Electronics,* vol. 28, no. 2: Optical Detectors, pp. 1-8, 2022, doi: 10.1109/JSTQE.2021.3129250.

[9] M. Wolf and D. Kress, "Short-range wireless infrared transmission: the link buoget compared to RF," *IEEE Wireless Communications,* vol. 10, no. 2, pp. 8-14, 2003, doi: 10.1109/MWC.2003.1196397.

[10] L. Feng, H. Yang, R. Q. Hu, and J. Wang, "MmWave and VLC-Based Indoor Channel Models in 5G Wireless Networks," *IEEE Wireless Communications,* vol. 25, no. 5, pp. 70-77, 2018, doi: 10.1109/MWC.2018.1600341.

[11] K. Ali *et al.*, "Measurement Campaign on 5G Indoor Millimeter Wave and Visible Light Communications Multi Component Carrier System," *IEEE Transactions on Broadcasting,* vol. 68, no. 1, pp. 156-170, 2022, doi: 10.1109/TBC.2021.3120918.

[12] A. Uyrus, B. Turan, E. Basar, and S. Coleri, "Visible Light and mmWave Propagation Channel Comparison for Vehicular Communications," in *2019 IEEE Vehicular Networking Conference (VNC)*, 4-6 Dec. 2019 2019, pp. 1-7, doi: 10.1109/VNC48660.2019.9062797.

[13] H. Abuella *et al.*, "Hybrid RF/VLC Systems: A Comprehensive Survey on Network Topologies, Performance Analyses, Applications, and Future Directions," *IEEE Access,* vol. 9, pp. 160402-160436, 2021, doi: 10.1109/ACCESS.2021.3129154.

[14] J. Y. Sung, E. Tangdiongga, and T. Koonen, "A Hybrid Radio-Optical Wireless System With Efficient Sub-Centimeter Localization for Full-Coverage Indoor Services," *Journal of Lightwave Technology,* vol. 39, no. 8, pp. 2368-2375, 2021, doi: 10.1109/JLT.2021.3052226.

[15] D. O'Brien, S. Rajbhandari, and H. Chun, "Transmitter and receiver technologies for optical wireless," *Philosophical Transactions of the Royal Society A: Mathematical, Physical and Engineering Sciences,* vol. 378, no. 2169, p. 20190182, 2020/03/02 2020, doi: 10.1098/rsta.2019.0182.

[16] S. J. Orfanidis, *Electromagnetic Waves and Antennas*, 2016. [Online]. Available: https://www.ece.rutgers.edu/~orfanidi/ewa/. Accessed on: 6/18/2023.

[17] S. Liu, X. Yu, R. Guo, Y. Tang, and Z. Zhao, "THz channel modeling: Consolidating the road to THz communications," *China Communications,* vol. 18, no. 5, pp. 33-49, 2021, doi: 10.23919/JCC.2021.05.003.

[18] V. Petrov, M. Komarov, D. Moltchanov, J. M. Jornet, and Y. Koucheryavy, "Interference and SINR in Millimeter Wave and Terahertz Communication Systems With Blocking and Directional Antennas," *IEEE Transactions on Wireless Communications,* vol. 16, no. 3, pp. 1791-1808, 2017, doi: 10.1109/TWC.2017.2654351.

[19] ITU-R, "Attenuation by atmospheric gases and related effects," *Recommendation ITU-R P.676-12,* 2019.

[20] A. A. A. Boulogeorgos, E. N. Papasotiriou, and A. Alexiou, "Analytical Performance Assessment of THz Wireless Systems," *IEEE Access,* vol. 7, pp. 11436-11453, 2019, doi: 10.1109/ACCESS.2019.2892198.

[21] E. N. Papasotiriou, A.-A. A. Boulogeorgos, K. Haneda, M. F. de Guzman, and A. Alexiou, "An experimentally validated fading model for THz wireless systems," *Scientific Reports,* vol. 11, no. 1, p. 18717, 2021/09/21 2021, doi: 10.1038/s41598-021-98065-x.

[22] J. G. Proakis and M. Salehi, *Digital Communications, 5th edition*. McGraw-Hill Higher Education, 2008.

[23] H. Haas, M. S. Islim, C. Chen, and H. Abumarshoud, *An Introduction to Optical Wireless Mobile Communication*. Artech House, 2021.

[24] Hamamatsu. "Si APD." https://www.hamamatsu.com/content/dam/hamamatsu-photonics/sites/documents/99_SALES_LIBRARY/ssd/si-apd_kapd9007e.pdf (accessed 6/18/2023.

[25] J. M. Kahn and J. R. Barry, "Wireless infrared communications," *Proceedings of the IEEE,* vol. 85, no. 2, pp. 265-298, 1997, doi: 10.1109/5.554222.

[26] M. Safari, "Efficient optical wireless communication in the presence of signal-dependent noise," in *2015 IEEE International Conference on Communication Workshop (ICCW)*, 8-12 June 2015 2015, pp. 1387-1391, doi: 10.1109/ICCW.2015.7247372.

[27] L. Zhang, H. Chun, G. Faulkner, D. O. Brien, and S. Collins, "A comparison between the sensitivities of VLC receivers containing an off-the-shelf SPAD array and an APD," in *2017 IEEE Photonics Conference (IPC)*, 1-5 Oct. 2017 2017, pp. 27-28, doi: 10.1109/IPCon.2017.8115990.

[28] Z. Ahmed, R. Singh, W. Ali, G. Faulkner, D. O'Brien, and S. Collins, "A SiPM-Based VLC Receiver for Gigabit Communication Using OOK Modulation," *IEEE Photonics Technology Letters,* vol. 32, no. 6, pp. 317-320, 2020, doi: 10.1109/LPT.2020.2973200.

[29] W. Matthews, Z. Ahmed, W. Ali, and S. Collins, "A 3.45 Gigabits/s SiPM-Based OOK VLC Receiver," *IEEE Photonics Technology Letters,* vol. 33, no. 10, pp. 487-490, 2021, doi: 10.1109/LPT.2021.3069802.

[30] Hamamatsu. "MPPC." https://www.hamamatsu.com/content/dam/hamamatsu-photonics/sites/documents/99_SALES_LIBRARY/ssd/mppc_kapd9005e.pdf (accessed 6/18/2023.

[31] L. Zhang *et al.*, "A Comparison of APD- and SPAD-Based Receivers for Visible Light Communications," *Journal of Lightwave Technology,* vol. 36, no. 12, pp. 2435-2442, 2018, doi: 10.1109/JLT.2018.2811180.

[32] L. Zhang, H. Chun, G. Faulkner, D. O. Brien, and S. Collins, "Efficient pulse amplitude modulation for SPAD-based receivers," in *2018 Global LIFI Congress (GLC)*, 8-9 Feb. 2018 2018, pp. 1-5, doi: 10.23919/GLC.2018.8319119.

[33] L. Zhang, H. Chun, Z. Ahmed, G. Faulkner, D. O. Brien, and S. Collins, "The Future Prospects for SiPM-Based Receivers for Visible Light Communications," *Journal of Lightwave Technology,* vol. 37, no. 17, pp. 4367-4374, 2019, doi: 10.1109/JLT.2019.2923957.

[34] S. Vinogradov, T. Vinogradova, V. Shubin, D. Shushakov, and K. Sitarsky, "Probability distribution and noise factor of solid state photomultiplier signals with cross-talk and afterpulsing," in *2009 IEEE Nuclear Science Symposium Conference Record (NSS/MIC)*, 24 Oct.-1 Nov. 2009 2009, pp. 1496-1500, doi: 10.1109/NSSMIC.2009.5402300.

[35] A. Buchner *et al.*, "Analytical Evaluation of Signal-to-Noise Ratios for Avalanche- and Single-Photon Avalanche Diodes," *Sensors*, vol. 21, no. 8, doi: 10.3390/s21082887.

[36] G. A. Mapunda, R. Ramogomana, L. Marata, B. Basutli, A. S. Khan, and J. M. Chuma, "Indoor Visible Light Communication: A Tutorial and Survey," *Wireless Communications and Mobile Computing,* vol. 2020, p. 8881305, 2020/12/11 2020, doi: 10.1155/2020/8881305.

[37] M. S. Islim and h. haas, "Modulation Techniques for Li-Fi," *ZTE COMMUNICATIONS,* vol. 14, pp. 29-40, 04/01 2016.

[38] *Standard Tables for Reference Solar Spectral Irradiances: Direct Normal and Hemispherical on 37° Tilted Surface*, ASTM.

[39] Hamamatsu. "Si APD S8664-10K." https://www.hamamatsu.com/us/en/product/optical-sensors/apd/si-apd/S8664-10K.html (accessed 6/9/2023.

[40] Onsemi. "Silicon Photomultipliers (SiPM), High PDE and Timing Resolution Sensors in a TSV Package - J-Series SiPM Sensors." https://www.onsemi.com/pdf/datasheet/microj-series-d.pdf (accessed 6/18/2023.

[41] J. R. Barry, *Wireless Infrared Communications*. Springer US, 1994.

[42] I. F. Akyildiz, C. Han, Z. Hu, S. Nie, and J. M. Jornet, "Terahertz Band Communication: An Old Problem Revisited and Research Directions for the Next Decade," *IEEE Transactions on Communications,* vol. 70, no. 6, pp. 4250-4285, 2022, doi: 10.1109/TCOMM.2022.3171800.

[43] *Study on support of reduced capability NR devices*, 3GPP TR 38.875 V17.0.0, March 2021.

[44] H. J. Song and N. Lee, "Terahertz Communications: Challenges in the Next Decade," *IEEE Transactions on Terahertz Science and Technology,* vol. 12, no. 2, pp. 105-117, 2022, doi: 10.1109/TTHZ.2021.3128677.

[45] J. Jeon, K. Muhammad, J. Cho, G. Xu, I. Na, and J. Zhang, "Design Considerations for Terahertz Wireless Communication Systems," in *2020 IEEE Wireless Communications and Networking Conference Workshops (WCNCW)*, 6-9 April 2020 2020, pp. 1-5, doi: 10.1109/WCNCW48565.2020.9124801.

[46] D. Lee, A. Davydov, B. Mondal, G. Xiong, G. Morozov, and J. Kim, "From sub-Terahertz to Terahertz: challenges and Design Considerations," in *2020 IEEE Wireless Communications and Networking Conference Workshops (WCNCW)*, 6-9 April 2020 2020, pp. 1-8, doi: 10.1109/WCNCW48565.2020.9124764.

[47] K. Kikuchi, "Fundamentals of Coherent Optical Fiber Communications," *Journal of Lightwave Technology,* vol. 34, no. 1, pp. 157-179, 2016, doi: 10.1109/JLT.2015.2463719.